A poroelastic model coupled to a fluid network with applications in lung modelling

Lorenz Berger[1], Rafel Bordas[1], Kelly Burrowes[1], Vicente Grau[2], Simon Tavener[3] and David Kay[1,*,†]

[1]*Department of Computer Science, University of Oxford, Wolfson Building Parks, Road, OX1 3QD, Oxford, UK*
[2]*Institute of Biomedical Engineering, Department of Engineering Science, Old Road Campus Research Building, University of Oxford, Headington, Oxford OX3 7DQ, UK*
[3]*Department of Mathematics, Colorado State University, Weber Building, Fort Collins, CO 80523, USA*

SUMMARY

We develop a lung ventilation model based on a continuum poroelastic representation of lung parenchyma that is strongly coupled to a pipe network representation of the airway tree. The continuous system of equations is discretized using a low-order stabilised finite element method. The framework is applied to a realistic lung anatomical model derived from computed tomography data and an artificially generated airway tree to model the conducting airway region. Numerical simulations produce physiologically realistic solutions and demonstrate the effect of airway constriction and reduced tissue elasticity on ventilation, tissue stress and alveolar pressure distribution. The key advantage of the model is the ability to provide insight into the mutual dependence between ventilation and deformation. This is essential when studying lung diseases, such as chronic obstructive pulmonary disease and pulmonary fibrosis. Thus the model can be used to form a better understanding of integrated lung mechanics in both the healthy and diseased states. Copyright © 2015 John Wiley & Sons, Ltd

1. INTRODUCTION

The main function of the lungs is to exchange gas between air and blood, supplying oxygen during inspiration and removing carbon dioxide by subsequent expiration. Gas exchange is optimised by ensuring efficient matching between ventilation and blood flow, the distributions of which are largely governed by the branching structure of the airway and vascular trees, tissue deformation and gravity. We focus on the coupling of tissue deformation and ventilation. Previous work of whole organ lung models has typically focused on modelling either ventilation or tissue deformation [1–8]. However, the two components are intrinsically linked; evaluating them separately does not necessarily provide an accurate description of lung function. To gain a better understanding of the biomechanics in the lung, it is therefore necessary to fully couple the tissue deformation with the ventilation. To achieve this tight coupling between tissue deformation and ventilation, we propose a novel model that approximates the lung parenchyma by a biphasic (tissue and air) poroelastic model that is coupled to an airway network model. A poroelastic model of lung parenchyma was first proposed in [9]. This model was applied in a very simple 2D geometrical domain. A homogenisation

---

approach was taken in [10] to derive macroscopic poroelastic equations for average air flows and tissue displacements in lung parenchyma under high-frequency ventilation.

The fully coupled poroelastic fluid-network model developed here has the potential to advance the understanding of the biomechanics of respiratory diseases. It takes advantage of realistic deformation boundary conditions and incorporates several generations of a realistic airway tree, both of which are obtained from imaging data. It has the ability to incorporate spatially varying material properties. An integrated model of ventilation and tissue mechanics is particularly important for understanding respiratory diseases because nearly all pulmonary diseases lead to some abnormality of lung tissue mechanics [11]. Chronic obstructive pulmonary disease encompasses emphysema, the destruction of alveolar tissue, as well as chronic bronchitis, which can cause severe airway remodelling, bronchoconstriction and air trapping. All of the aforementioned affect tissue deformation because sections of lung are either not able to expand to inspire air, or to contract to release air. The effects of physiological changes occurring during disease, such as airway narrowing and changes in tissue properties, on regional ventilation and tissue stress are not well understood. For example, one hypothesis is that airway disease may precede emphysema [12]. An integrated model of ventilation and tissue mechanics can be used to investigate the impact of airway narrowing and tissue stiffness during obstructive lung diseases on tissue stresses, alveoli pressure and ventilation.

Ventilation models that incorporate many independent elastic alveolar units, e.g. [1, 2] are commonly known as balloon models. In these models, alveolar units can expand and contract independently of the sizes and positions of neighbouring units, which can lead to unphysical solutions in which multiple balloons apparently occupy the same location in space. In reality, acini do not function as independent elastic balloons [13]. They are physically coupled through fibrous scaffolding and shared alveolar septa. In Figure 1, we illustrate this issue by comparing two simplistic balloon models. Our model does not suffer from this difficulty.

Lung models [1, 2] provide information regarding the distribution of flow within the lung as a result of a pleural pressure boundary condition. However, it is not possible to experimentally measure the pleural pressure *in vivo* using imaging or other apparatus. As part of the simulation protocol, the pleural pressure is therefore often tuned until physiological realistic flow rates are achieved. To overcome this issue, [14, 15] proposed to estimate the flow boundary conditions for full organ ventilation models by means of image registration. However, by relying on image registration to determine the ventilation distribution within the tissue, one is not able to model the change in ventilation distribution because of progression of disease. Following the approach in [15], we integrate image registration-based boundary conditions within the proposed poroelastic model of lung deformation. In particular, we register expiratory images to the inspiratory images to yield an estimate of the deformation boundary condition for the lung surface, and drive the simulation through this deformation boundary condition. The tissue deformation and subsequent flow boundary condition for tree branches inside the lung and ventilation distribution is not pre-determined, but calculated from the coupled poroelastic-airway-tree model. Thus the model provides realistic deformation of lung whilst allowing flexibility to investigate how ventilation changes in response to changes in tissue properties.
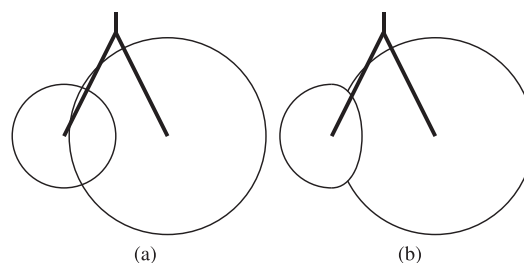

(a)   (b)

Figure 1. Sketch of two balloon models where the right alveolar unit is more compliant. (a) Balloon model with independent alveolar units. The overlap is physically unrealistic. (b) Balloon model where the alveolar units are coupled. Here, the inflation of each alveolar unit is compromised by the expansion of its neighbour.

The rest of this paper is organised as follows. In Section 2, we present the assumptions inherent in a poroelastic model for the lung. We develop a poroelastic lung model in Section 3, discuss its discretization in Section 4 and describe the generation of realistic boundary and initial conditions in Section 5. We present numerical simulations of tidal breathing in Section 6 and investigate the effect of airway constriction and tissue weakening. Finally, we draw some conclusions in Section 7.

2. MODELING LUNG PARENCHYMA AS A (CONTINUOUS) POROELASTIC MATERIAL

In order to make a computationally tractable lung model, we assume that we can approximate the lung parenchyma as a (continuous) poroelastic material and couple this to an airway network. The use of a continuum model can be supported by consideration of the different length scales and structures of the tissue. For the microscopic length scale, denoted by l, we will use the diameter of an alveolus, which is approximately 0.02 cm [16]. The macroscopic length scale L can be taken to be the diameter of a lung segment, which measures around 4 cm. The ratio of the different length scales is therefore $\epsilon := \frac{l}{L} \approx 0.005 \ll 1$. This, together with the assumption that the structure of an acinus is porous (Figures 2(a) and 2(b)) and approximately periodic, supports the use of averaging techniques over the tissue to obtain a continuum description in the form of a poroelastic medium. By averaging over the tissue, we do not seek to model individual alveoli but introduce macroscopic parameters such as the permeability and elasticity coefficients. In general, lung diseases affect significant regions of alveoli (lung tissue), and thus, by changing the macro-scale parameters over the affected area of tissue we are able to model changes in the tissue due to disease.

We make the following assumptions.

(a) Blood is simply part of the tissue. The volume occupied by blood in the capillaries is similar to the volume occupied by collagen and elastin fibres (illustrated in Figure 2(a)). The space not occupied by air is about 7% of the parenchymal volume and is made up of 50% capillary blood and 50% of collagen and elastin fibres [17]. Further, the density of blood is similar to the density of tissue and much larger than that of air ($1060 \, kg \, m^{-3} \gg 1.18 \, kg \, m^{-3}$).

(b) Both the solid phase (blood and tissue) and a fluid phase (air) are incompressible [1].

(c) Accelerations of the solid phase in the poroelastic medium are negligible and will be ignored. Calculations of the sinusoidal motion of tissue near the diaphragm during normal breathing yield an estimate of $0.02 \, ms^{-2}$ for the maximum acceleration of lung parenchyma, which is negligible compared with the acceleration of gravity

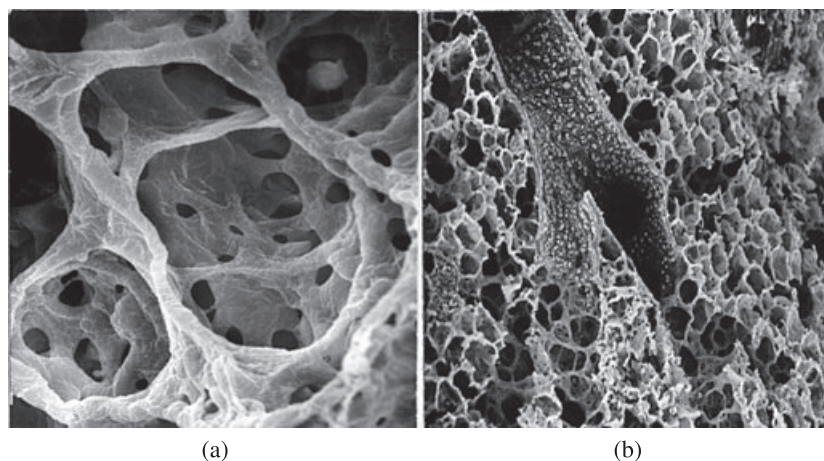(a)   (b)

Figure 2. (a) Alveoli in an alveolar duct. The dark round openings are pores between alveoli. The alveolar wall is quite thin and contains a network of capillaries. The average diameter of one alveoli is 0.2 mm. (b) Transition from terminal bronchiole to alveolar duct, from conducting airway to oxygen transfer area, diameter of terminal bronchiole is 0.5 mm. Images are reproduced from [18].

(d) We ignore accelerations of the fluid phase within the poroelastic medium [19]. The Reynolds number in the lower airways that form part of the lung parenchyma has been estimated to be between 0.01 and 1 [20].

(e) We neglect the fluid viscous stress. A dimensional analysis [21] shows that when the microscopic and macroscopic length scales are widely separated, the internal viscous stresses in the fluid are small compared with the drag forces between the fluid and the porous structure.

(f) The flow in the airways is laminar (Poiseuille) flow [2, 22]. Diseases affecting the airway tree will be modelled effectively by changing resistance (airway radius) parameters in the network flow model.

3. THE POROELASTIIC LUNG MODEL

A detailed description and full derivation of the poroelastic equations can be found in [23] and [24].

3.1. The poroelastic model for lung parenchyma

Consistent with the usual conventions, we use X and x to denote position in the reference and deformed domains $\Omega(0)$ and $\Omega(t)$, respectively, and specify the poroelastic model as follows: find displacement $\chi(X, t)$, fluid flux $z(x, t)$ and pressure $p(x, t)$ such that

$$\left.\begin{array}{rl}
-\nabla \cdot (\sigma_e - pI) = \rho f & \text{in } \Omega(t), \\
k^{-1}z + \nabla p = \rho^f f & \text{in } \Omega(t), \\
\nabla \cdot (\chi_t + z) = g & \text{in } \Omega(t), \\
\chi(X, t)|_{X=\chi^{-1}(x,t)} = X + u_D & \text{on } \Gamma_d(t), \\
(\sigma_e - pI)n = t_N & \text{on } \Gamma_n(t), \\
z \cdot n = q_D & \text{on } \Gamma_f(t), \\
p = p_D & \text{on } \Gamma_p(t), \\
\chi(X, 0) = X & \text{in } \Omega.
\end{array}\right\}, \tag{1}$$

where $\chi(X, t)$ is the continuously differentiable, invertible deformation from $\Omega(0)$ to $\Omega(t)$, $z = \phi(v^f - v^s)$ is the fluid flux where v^f and v^s are the velocities of the fluid and solid components, respectively, $\phi(x, t)$ is the volume fraction of fluid and σ_e is the stress tensor given by

$$\sigma_e = \frac{1}{J} F \cdot 2 \frac{\partial W(C)}{\partial C} \cdot F^T. \tag{2}$$

Here, $F = \dfrac{\partial \chi(X, t)}{\partial X}$, $J = \det(F)$, $C = F^T F$ and $\rho = \rho^s(1 - \phi) + \rho^f \phi$, where ρ^s and ρ^ϕ are the densities of the solid and fluid components, respectively. We implemented the Neo–Hookean strain-energy law $W(C)$ proposed in [25]

$$W(C) = \frac{\mu}{2}(\text{tr}(C) - 3) + \frac{\lambda}{4}(J^2 - 1) - (\mu + \frac{\lambda}{2})\ln(J - 1 + \phi_0), \tag{3}$$

with the penalty term chosen such that $0 \leq \phi < 1$.

The permeability tensor $k = J^{-1}F k_0(C) F^T$, where $k_0(C)$ is the permeability in the reference configuration. Examples of deformation dependent permeability tensors for biological tissues can be found in [26–28]. We implemented the law proposed in [26] to model lung parenchyma

$$k_0 = k_0 \left(J \frac{\phi}{\phi_0} \right)^{2/3} I. \tag{4}$$

Finally, the boundary is partitioned as $\partial\Omega(t) = \Gamma_d(t) \cup \Gamma_n(t)$ for the mixture and $\partial\Omega(t) = \Gamma_p(t) \cup \Gamma_f(t)$ for the fluid, with an outward pointing unit normal $\boldsymbol{n}$.

3.2. Network flow model for the airway tree

The flow rate Q_i through the ith segment in the airway network is given by the pressure–flow relationship

$$P_{i,1} - P_{i,2} = R_i Q_i, \tag{5}$$

where $R_i = \dfrac{8l\mu_f}{\pi r^4}$ is the Poiseuille flow resistance of a pipe segment where r and l are the radius and length of the pipe, μ_f is the dynamic viscosity, and $P_{i,1}$ and $P_{i,2}$ are the pressures at the proximal and distal nodes of the pipe segment, respectively. Let A_i be the set of pipe segments emanating from the ith pipe segment in the airway network. We can express the conservation of flow in the airway network as

$$Q_i = \sum_{j \in A_i} Q_j. \tag{6}$$

The outlet pressure of the airway network is set using the boundary condition $P_0 = \hat{P}$.

3.2.1. Coupling the airway network to the poroelastic model.
We introduce subdomains to identify the region of the domain that is supplied with fluid from a specific branch of the airway network and returns fluid through that branch. For notational purposes, we use the subscript di to indicate the most distal branches that have no further conducting branches emanating from them, but which enter a group of acinar units approximated by the continuous poroelastic model. We construct a Voronoi tesselation based on the N terminal locations $\boldsymbol{y}_{di}, i = 1, \ldots, N$ of the airway network. The ith subdomain $\Omega_i(t)$ is the subset of Ω that is closer the ith terminal location at $\boldsymbol{y}_{di}$ than to any of the other terminal locations, i.e.

$$\Omega_i(t) := \left\{ \boldsymbol{x} \in \Omega(t) : ||\boldsymbol{x} - \boldsymbol{y}_i|| < ||\boldsymbol{x} - \boldsymbol{y}_j||, \ j = 1, 2..., N \ , j \neq i \right\}, \quad i = 1, \ldots, N. \tag{7}$$

Obviously, we have $\overline{\Omega}(t) = \bigcup \overline{\Omega}_i(t)$. A simple 2D example is shown in Figure 3.

We couple the airway network to the poroelastic domain in two ways. Firstly, the flux from each distal airway acts as a source term in the poroelastic mass conservation equation, namely,

$$\nabla \cdot (\boldsymbol{\chi}_t + \boldsymbol{z}) = Q_{di} \quad \text{in } \Omega_i(t). \tag{8}$$

Secondly, the pressure at the distal airway, P_{di}, determines the average pressure within subdomain $\Omega_i(t)$, i.e.

$$\frac{1}{|\Omega_i(t)|} \int_{\Omega_i(t)} p \, \mathrm{d}\Omega_i(t) = P_{di}, \tag{9}$$

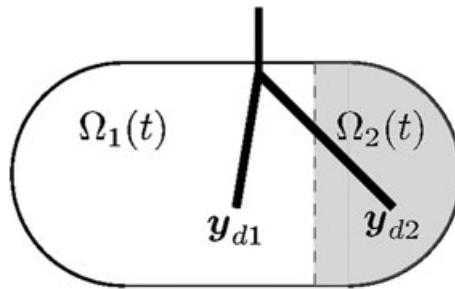where $|\Omega_i(t)|$ denotes the volume of the subdomian $\Omega_i(t)$.

Figure 3. A simple example of a 2D domain being split into two subdomains according to [7].

3.3. The coupled lung parenchyma/airway model

The coupled poroelastic-fluid-network lung model is as follows: find $\chi(X,t)$, $z(x,t)$, $p(x,t)$, P_i and Q_i such that

$$
\left.
\begin{aligned}
-\nabla \cdot (\sigma_e - pI) &= \rho f \quad \text{in } \Omega(t), \\
k^{-1}z + \nabla p &= \rho^f f \quad \text{in } \Omega(t), \\
\nabla \cdot (\chi_t + z) &= Q_{di} \quad \text{in } \Omega_i(t), \\
\chi(X,t)|_{X=\chi^{-1}(x,t)} &= X + u_D \quad \text{on } \Gamma_d(t), \\
(\sigma_e - pI)n &= t_N \quad \text{on } \Gamma_n(t), \\
z \cdot n &= q_D \quad \text{on } \Gamma_f(t), \\
p &= p_D \quad \text{on } \Gamma_p(t), \\
\chi(X,0) &= X, \quad \text{in } \Omega(0), \\
P_0 &= \hat{P}, \\
P_{i,1} - P_{i,2} &= R_i Q_i, \\
Q_i &= \sum_{j \in A_i} Q_j, \\
\frac{1}{|\Omega_i(t)|} \int_{\Omega_i(t)} p \, d\Omega_i(t) &= P_{di},
\end{aligned}
\right\}, \tag{10}
$$

where $\partial\Omega(t) = \Gamma_d(t) \cup \Gamma_n(t)$ for the mixture and $\partial\Omega(t) = \Gamma_p(t) \cup \Gamma_f(t)$ for the fluid, with an outward pointing unit normal n.

4. NUMERICAL SOLUTION OF THE POROELASTIC LUNG MODEL

4.1. Discretization of the poroelastic equations

The poroelastic equations (1) are discretized in space using the finite element method. We use a stabilised mixed finite element $P1 - P1 - P0$, which uses continuous piecewise linear approximations for both the fluid flux and deformation and piecewise constant approximation for the pressure space. The stabilisation scheme is analysed in [29]. The temporal discretisation is achieved by taking a standard backward Euler approach. Let ϕ_k denote a vector-valued linear basis function, ψ_i a scalar-valued piecewise constant basis function and ϵ_k a scalar-valued linear basis function and define

$$
\chi_i^n = \sum_{k=1}^{n_\chi} \chi_{i,k}^n \phi_k, \quad z_i^n = \sum_{k=1}^{n_z} z_{i,k}^n \phi_k, \quad p_i^n = \sum_{k=1}^{n_p} p_{i,k}^n \psi_k, \quad \Lambda_i^n = \sum_{k=1}^{n_\Lambda} \Lambda_{i,k}^n \epsilon_k,
$$

where Λ is the Lagrange multiplier associated with the fluid flux boundary condition ([23] for details).

4.2. Coupling of the fluid network to the discretized poroelastic model

To illustrate our approach, consider the discretization of the 2D domain using triangular elements in Figure 4(a) and (b). The ith discretized subdomain $\Omega_i(t)$ is defined as the set of elements E_k whose centroids $\overline{x_k}$ are closer to the distal end of the ith terminal branch than to the distal end of any other terminal branch, i.e.

$$
\Omega_i(t) := \left\{ E_k \in \Omega(t) : \|\overline{x_k} - y_{di}\| < \|\overline{x_k} - y_{dj}\|, \ j = 1, 2 ..., N, \ j \neq i \right\}. \tag{11}
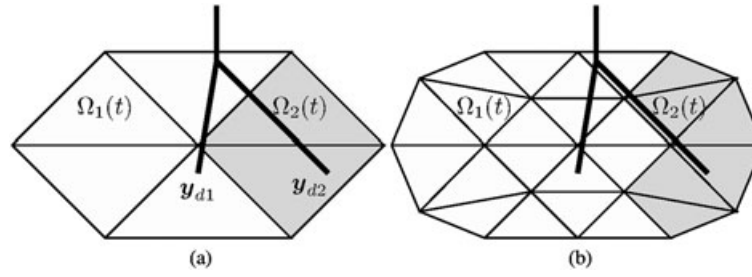$$

Figure 4. (a) Coupling between the discretized domain and the airway network for the example shown in Figure 3. (b) Coupling between the discretized domain and the airway network after mesh refinement.

The discretized subdomains converge towards the subdomains defined by (7) as the mesh is refined.

Let $\mathbf{P}^n$ and $\mathbf{Q}^n$ be the pressures at each junction and the fluid fluxes in each branch of airway network, except for the pressures at the distal end of, and the fluxes in, the most distal branches of the airway network which are given by $\mathbf{P}_d^n$ and $\mathbf{Q}_d^n$, respectively.

4.3. Discretization and solution via Newton's method

A Newton algorithm defined in [23] is used to solve the system of equations at each particular time step n. Let u_i^n denote the fully discrete solution of the coupled problem at the ith step within the Newton method at time t^n. For the coupled poroelastic and airway network model, we solve a linear system of the form

$$\boldsymbol{K}(u_i^n)\delta u_{i+1}^n = -\boldsymbol{R}\left(u_i^n, u^{n-1}\right) \tag{12}$$

at each Newton iteration, where $\boldsymbol{K}$ is the approximate linearization of the nonlinear system of equations and $\boldsymbol{R}$ is the residual vector. In particular,

$$
\begin{bmatrix}
\mathbf{K}^e & 0 & \mathbf{B}^T & 0 & 0 & 0 & 0 & 0 \\
0 & \mathbf{M} & \mathbf{B}^T & \mathbf{L}^T & 0 & 0 & 0 & 0 \\
-\mathbf{B} & -\Delta t\mathbf{B} & \mathbf{J} & 0 & 0 & 0 & 0 & -\Delta t\mathbf{G}^T \\
0 & \mathbf{L} & 0 & 0 & 0 & 0 & 0 & 0 \\
0 & 0 & 0 & 0 & \mathbf{T}_{11} & \cdots & \cdots & \mathbf{T}_{14} \\
0 & 0 & 0 & 0 & \vdots & & & \vdots \\
0 & 0 & 0 & 0 & \mathbf{T}_{31} & \cdots & \cdots & \mathbf{T}_{34} \\
0 & 0 & \mathbf{G} & 0 & 0 & -\mathbf{X} & 0 & 0
\end{bmatrix}
\begin{bmatrix}
\delta\boldsymbol{\chi}^n \\
\delta\mathbf{z}^n \\
\delta\mathbf{p}^n \\
\delta\boldsymbol{\Lambda}^n \\
\delta\mathbf{P}^n \\
\delta\mathbf{P}_d^n \\
\delta\mathbf{Q}^n \\
\delta\mathbf{Q}_d^n
\end{bmatrix}
= -
\begin{bmatrix}
\boldsymbol{r}_1 \\
\boldsymbol{r}_2 \\
\boldsymbol{r}_3 - \Delta t\mathbf{G}^T\mathbf{Q}_d^n \\
0 \\
0 \\
0 \\
0 \\
\mathbf{G}\mathbf{p}^n - \mathbf{X}\mathbf{P}_d^n
\end{bmatrix},
$$

where

$$k_{kl}^e = \int_{\Omega(t_n)} \left[\boldsymbol{E}_k^T \boldsymbol{D}\left(\chi_i^n\right) \boldsymbol{E}_l + (\nabla\boldsymbol{\phi}_k)^T \boldsymbol{\sigma}_e\left(\chi_i^n\right) \nabla\boldsymbol{\phi}_l \right] \mathrm{d}\Omega(t_n),$$

$$m_{kl} = \int_{\Omega(t_n)} k^{-1}(\chi_i^n)\boldsymbol{\phi}_k \cdot \boldsymbol{\phi}_l \, \mathrm{d}\Omega(t_n),$$

$$b_{kl} = -\int_{\Omega(t_n)} \psi_k \nabla \cdot \boldsymbol{\phi}_l \, \mathrm{d}\Omega(t_n),$$

$$j_{kl} = \Upsilon \sum_{K \in \mathcal{T}_i^h} \int_{\partial K \setminus \partial\Omega(t_n)_i} h_{\partial K} [\![\psi_k]\!] [\![\psi_l]\!] \, \mathrm{d}s.$$

$$r_{1i} = \int_{\Omega(t_n)} \left[(\boldsymbol{\sigma}_e(\chi_i^n) - p_i^n \boldsymbol{I}) : \nabla\boldsymbol{\phi}_i - \rho(\chi_i^n)\boldsymbol{\phi}_i \cdot \boldsymbol{f} \right] \mathrm{d}\Omega(t_n) - \int_{\Gamma_n(t_n)} \boldsymbol{\phi}_i \cdot \boldsymbol{t}_N(\chi_i^n) \, \mathrm{d}\Gamma_n(t_n),$$

$$r_{2i} = \int_{\Omega(t_n)} \left[k^{-1}(\chi_i^n)\boldsymbol{\phi}_i \cdot z_i^n - p_i^n \nabla \cdot \boldsymbol{\phi}_i - \rho^f(\chi_i^n)\boldsymbol{\phi}_i \cdot \boldsymbol{f} \right] \, d\Omega(t_n),$$

$$r_{3i} = \int_{\Omega(t_n)} \psi_i \left[\nabla \cdot (\chi_i^n - \chi^{n-1}) + \Delta t \psi_i \nabla \cdot z_i^n - \Delta t \psi_i g \right] \, d\Omega(t_n)$$

$$+ \Upsilon \sum_{K \in \mathcal{T}^h} \int_{\partial K \backslash \partial \Omega(t_n)} h_{\partial K} [\![\psi_i]\!] [\![p_i^n - p^{n-1}]\!] \, ds,$$

$$\mathbf{l}_{ij} = \int_{\Omega(t_n)} \epsilon_i \boldsymbol{\phi}_j \cdot \boldsymbol{n}, \, d\Omega(t_n),$$

$$\mathbf{x}_{ij} = \begin{cases} 1 \text{ if } ||\boldsymbol{y}_{di} - \overline{\boldsymbol{x}_j}|| < ||\boldsymbol{y}_{dk} - \overline{\boldsymbol{x}_j}||, k = 1, 2 ..., N, k \neq i, \\ 0 \text{ otherwise,} \end{cases}$$

$$\mathbf{g}_{ij} = \int_{\Omega(t_n)} \mathbf{x}_{ij} \frac{\boldsymbol{\phi}_j}{|E_j|} \, d\Omega(t_n),$$

and $\mathbf{T}$ represents the matrix entries arising from equations (5) and (6). The matrix stabilisation block $\boldsymbol{J}$, jump operator $[\![\cdot]\!]$, stabilisation parameter Υ, diameter (3D) of the Kth element $h_{\partial K}$ and the matrices $\boldsymbol{D}$ and $\boldsymbol{E}$ are defined in [23, 29]. Finally, $\overline{\boldsymbol{x}_j}$ denotes the centroid of the jth element. As discussed in [23], our linearization is approximate because only the elasticity term is treated as a nonlinearity.

5. LUNG STRUCTURE AND MODELLING PARAMETERS

5.1. Mesh generation

We developed the geometry of a whole organ model of the right lung from high-resolution CT images taken at total lung capacity (TLC) and at functional residual capacity (FRC). The lung was first segmented from the CT data (slice thickness and pixel size 0.73 mm) using the commercially available segmentation software Mimics[1], and we then used the open-source image processing toolbox iso2mesh [30] to generate a Tetrahedral mesh containing 38 369 elements. The conducting airways were also segmented from the CT data taken at TLC, and a centerline with radial information was calculated. To approximate the remaining airways up to generation 8–13, we used a volume filling airway generation algorithm to generate a mesh of the airway tree containing 13 696 nodes with 2140 terminal branches [31].

5.2. Reference state, initial conditions and boundary conditions

The poroelastic framework we have described requires a stress free reference state. In general, biological tissues do not possess a 'reference state' where the material is free of both stress and strain, rather the cells that make up tissues are born into stressed states and live out their lives in these stressed states [32]. In order to define a stress-free reference state, we scale the lung from FRC to a configuration in which the internal stresses and strains are assumed to be zero. The lung model is then uniformly inflated from the reference state to create a pre-stressed FRC configuration, which has a mean elastic recoil of approximately 0.49×10^3 Pa, commonly understood to be a typical value [33]. Thus the displacement of the boundary required to get from the reference state to FRC is given by

$$\boldsymbol{u}_{D,FRC} = (s-1)\boldsymbol{X}, \tag{13}$$

where s is a scaling factor and $\boldsymbol{X}$ is the position of the lung surface in the reference state. From there, we simulate tidal breathing. A similar approach has also been used in [8].

We register the expiratory (FRC) segmentation to the segmentation at TLC using a very simple procedure that uses independent scalings a_1, a_2 and a_3 in the x, y and z direction, respectively, to

---

[†]http://biomedical.materialise.com/mimics.

Table I. Simulation parameters.

Parameter	Value	Reference
ϕ_0	0.99	[35]
κ_0	10^{-5} m^3 s kg^{-1}	[35]
E	0.73×10^3 Pa	[36]
ν	0.3	[36]
μ_f	1.92×10^{-5} kg m^{-1} s^{-1}	[2]
T	8 s	—
Δt	0.2 s	—
Υ	10^{-5}	—

map between the bounding boxes of the segmentations at FRC and TLC. This allows an estimate of the displacement for the lung surface from expiration to inspiration to be given by

$$\boldsymbol{u}_{D,TLC} = \begin{bmatrix} a_1 - 1 & 0 & 0 \\ 0 & a_2 - 1 & 0 \\ 0 & 0 & a_3 - 1 \end{bmatrix} (X + \boldsymbol{u}_{D,FRC}) + \boldsymbol{b}, \tag{14}$$

where $\boldsymbol{b}$ is a translation vector to ensure that the top of the lung stays pinned throughout the simulation. To simulate tidal breathing, we assume a sinusoidal breathing cycle and expand the lung surface from FRC to 40% of the displacement from FRC to TLC. Specifically,

$$\boldsymbol{u}_D(t) = \boldsymbol{u}_{D,FRC} + 0.2 \left(1 + \sin\left(\frac{\pi}{2}(t+3)\right)\right) \boldsymbol{u}_{D,TLC} \quad \text{on } \Gamma_d(t). \tag{15}$$

This results in a physiologically realistic tidal volume of 0.59 L at a breathing frequency of 15 breaths per minute. We simulate breathing for a total of 8 s or two breathing cycles. Because of the incompressibility of the poroelastic tissue, this also determines the total volume of air inspired/expired and the flowrate at the trachea, see Figure 6(a) and (b), respectively. We assume that no fluid escapes from the lung (except via the trachea) and impose zero flux boundary conditions at the lung surface. The outlet pressure of the airway network is set to zero (atmospheric pressure).

5.3. Simulation parameters

Several parameters for lung tissue elasticity and poroelasticity have been proposed [5, 10, 34–36], although there is no consensus in the values in the literature. In this study, we have chosen parameters as shown in Table I, which result in physiologically realistic simulations.

6. MODEL EXPLORATION

In the subsequent analysis, the total and elastic stress is calculated as $\sqrt{\lambda_1^2 + \lambda_2^2 + \lambda_3^2}$, where $\lambda_1, \lambda_2, \lambda_3$ are the three eigenvalues of the stress tensor. We define the relative Jacobian $J_V = J/J_{FRC}$, which is the volume ratio between the current state and FRC, as a measure for ventilation. Running simulations over many breaths, we found that differences between the second breath and subsequent breaths were negligible, and we therefore present results from the second breath, $t = 4$ s to $t = 8$ s. Unless otherwise stated, all subsequent figures that do not explicitly state the time are taken at $t = 5.8$ s, just before peak inhalation of the second time breath of the simulation. The sagittal slices used in subsequent figures is shown in Figure 5(a).

6.1. Normal breathing

To simulate tidal breathing, we apply the boundary conditions and simulation parameters previously discussed in Sections 5.2 and 5.3, respectively.

Figure 6 details the lung tidal volume, flow rate and pressure drop obtained from simulations of tidal breathing. Because of the incompressibility of the poroelastic medium and the fixed nature of the airway network, the lung tidal volume (Figure 6(a)) and flow rate (Figure 6(b)) follow

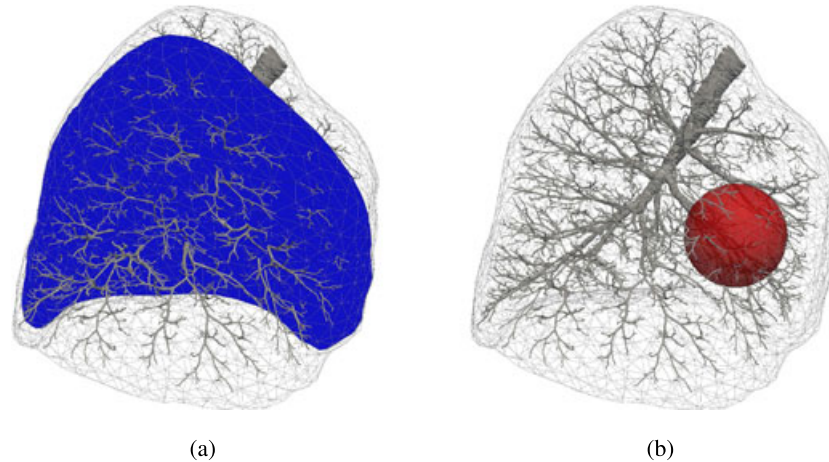(a)   (b)

Figure 5. (a) The blue sagittal slice indicates the position of subsequent slices used for the data analysis of the tissue. (b) The red ball represents the structurally modified region used to prescribe airway constriction and tissue weakening.
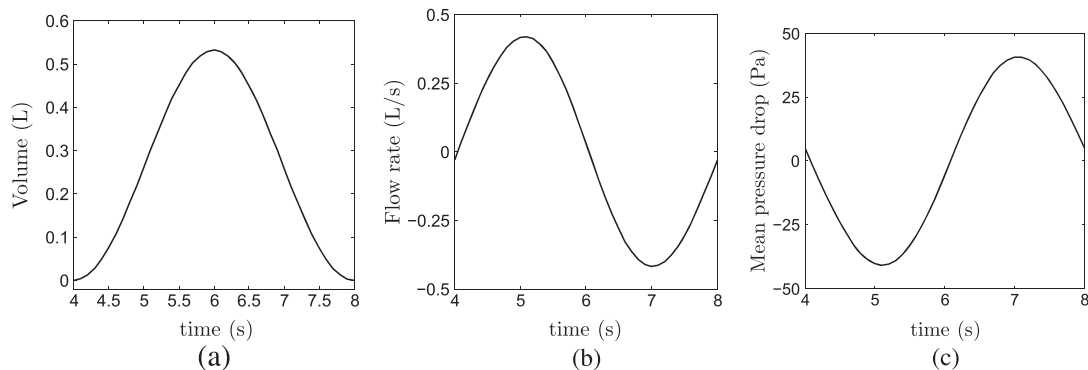

(a)   (b)   (c)

Figure 6. Simulated natural tidal breathing. (a) Lung tidal volume (volume increase from functional residual capacity), (b) flow rate at the inlet and (c) mean pressure drop from the inlet to the most distal branches.

a sinusoidal pattern that matches the form of the deformation boundary condition prescribed by equation (15). The mean pressure drop in the airways is shown in Figure 6(c) and agrees with previous simulation studies on full airway trees [1, 2].

The airway resistance (Poiseuille flow resistance) from the inlet (right bronchus) to each terminal airway is shown in Figure 7(a) for the entire airway. In Figure 7(b), we show the airway resistance of the terminal airways mapped onto the tissue.

In order to quantify the contribution of airway resistance to tissue expansion (ventilation), measured by J_V, the correlations between airway resistance in the tissue and J_V are plotted for each element in Figure 8(a). There is a clear correlation between airway resistance and tissue expansion, as is expected because the elastic coefficients are constant throughout the lung model. The Pearson correlation coefficients is -0.55; hence, ventilation decreases as airway resistance increases, with a p-value < 0.0001. Figure 8(b) shows there is also a strong correlation between the airway resistance and pressure in the poroelastic tissue. Here, the Pearson correlation coefficients is also -0.55, and pressure decreases (becomes more negative) with airway resistance, with a p-value < 0.0001. Note that for a very few regions that are coupled to terminal branches with a low airway resistance, positive pressures are possible. This results in a pressure gradient that pushes fluid from these well-ventilated regions to neighbouring less-ventilated regions, collateral ventilation [37].

The corresponding distribution of pressure in the airway tree is shown in Figure 9(a), and the pressure inside the poroelastic tissue is shown in Figure 9(b). Figure 9(c) shows the pressure on
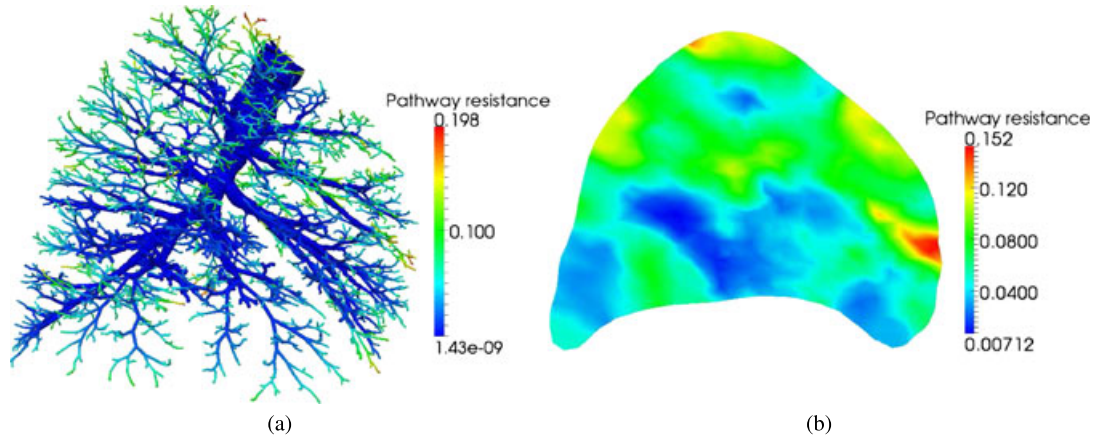
Figure 7. (a) Pathway resistance (Pa mm^{-3}s) from the inlet to the terminal branches in the airway tree and (b) pathway resistance mapped onto a slice of tissue.
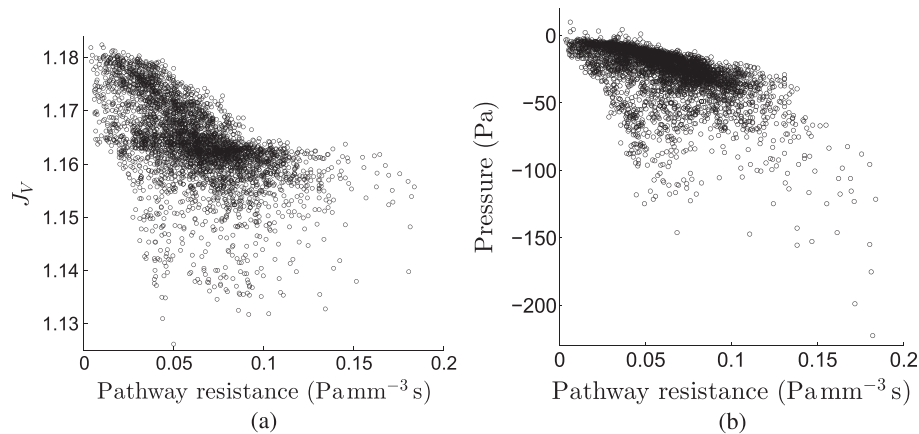

Figure 8. (a) Tissue expansion J_V versus resistance of the pathways from the inlet to the terminal branch and (b) pressure in the poroelastic medium (alveolar pressure) versus airway resistance.

the lung surface. The patchy pressure field is well approximated by the piecewise constant pressure elements employed by the finite element method used to solve the poroelastic equations ([23]). Figure 9(d) shows the distribution of tissue expansion.

6.2. Breathing with airway constriction

We simulate localised constriction of the airways by reducing the radii of the lower airways, here airways with radius less than 4 mm, within a ball near the right middle lobe. This region is represented by the red ball in Figure 5(b). Reducing the radius increases airway resistance per unit length. We reduce the radius of the lower airways with radii less than 4 mm by 0%, 40%, 50%, 60% and 65%. This corresponds to a mean airway resistance within the ball of 0.0507, 0.112, 0.188, 0.399 and 0.651 Pa mm^{-3}s, respectively. Mean tissue expansion during inspiration decreases as the airways become constricted as shown in Figure 10(a). The standard deviation of local tissue expansion increases because the airway resistance of each branch increases by a different amount depending on its original length and radius. Long and narrow branches are affected most by the constriction. Because a larger pressure drop is needed to force the air down the constricted branches, the pressure decreases with increasing airway resistance as shown in Figure 10(b). Figure 10(c) shows the elastic stress in the tissue decreases as airway resistance increases because of the decrease in tissue deformation (strain).
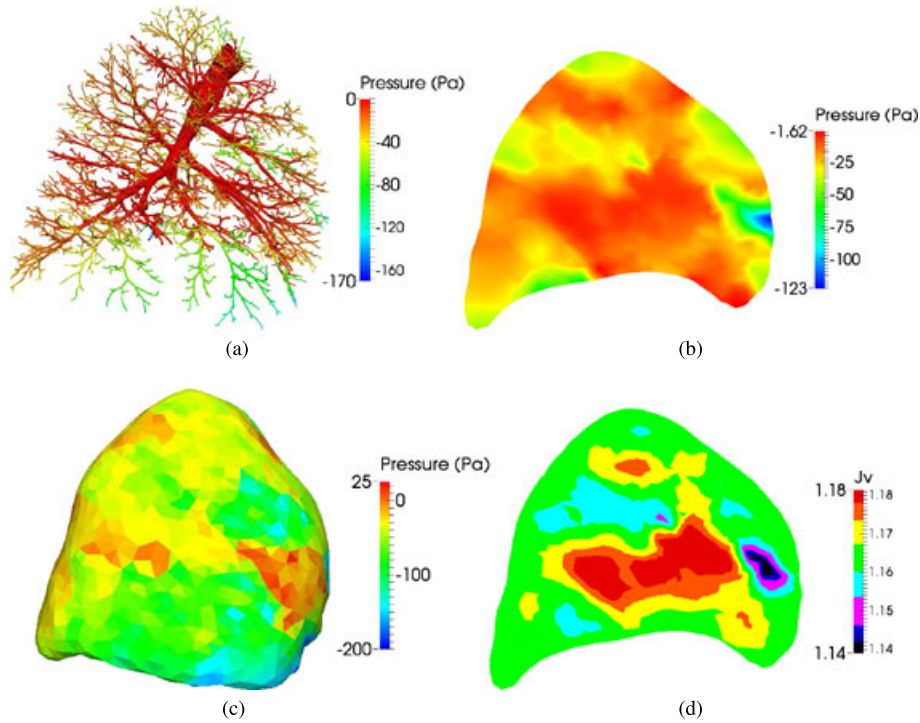
Figure 9. (a) Pressure in the airway tree, (b) tissue pressure on the sagittal slice, (c) pressure on the lung surface and (d) tissue expansion from functional residual capacity on the sagittal slice.
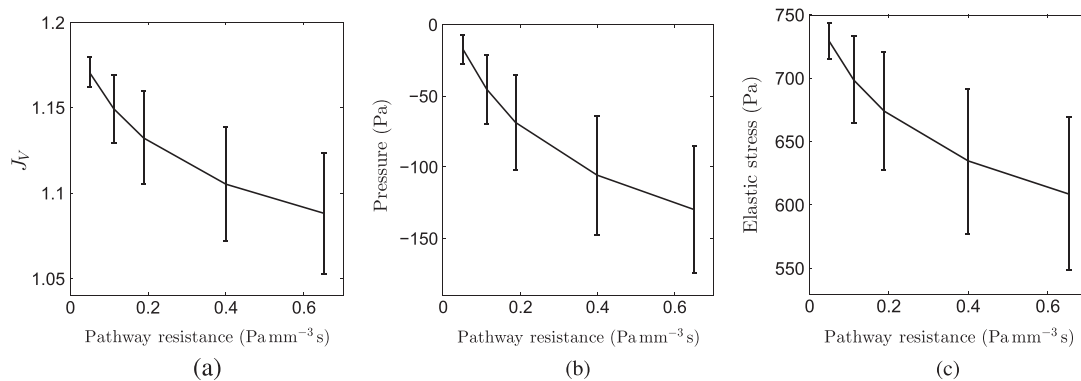

Figure 10. Global effects of increasing airway resistance within the modified region. (a) Means and standard deviations of tissue expansion, J_v, (b) means and standard deviations of tissue pressures and (c) means and standard deviations of elastic stresses.

The simulations results shown in Figure 11 were performed with 65% airway constriction in the lower airways within the structurally modified region. The local volume conserving property (mass conservation) of the method is illustrated in Figure 11(a), where the tissue surrounding the constricted area is expanding to compensate for the reduction of tissue expansion due to the constriction within the structurally modified region. However, as seen in Figure 11(c), a large elastic stress occurs near the boundary of the constricted region because of the difference in the relative expansions between the tissue within the modified region and the surrounding tissue. Figure 11(b) shows an increase in pressure near the boundary of this region. This facilitates air flow into the constricted region (collateral ventilation) to partially compensate for the reduced amount of ventilation, as is shown in Figure 11(d). The magnitude of the maximum flow within the tissue is 8×10^{-4} ms^{-1} is quite small because of the low permeability of the poroelastic material.
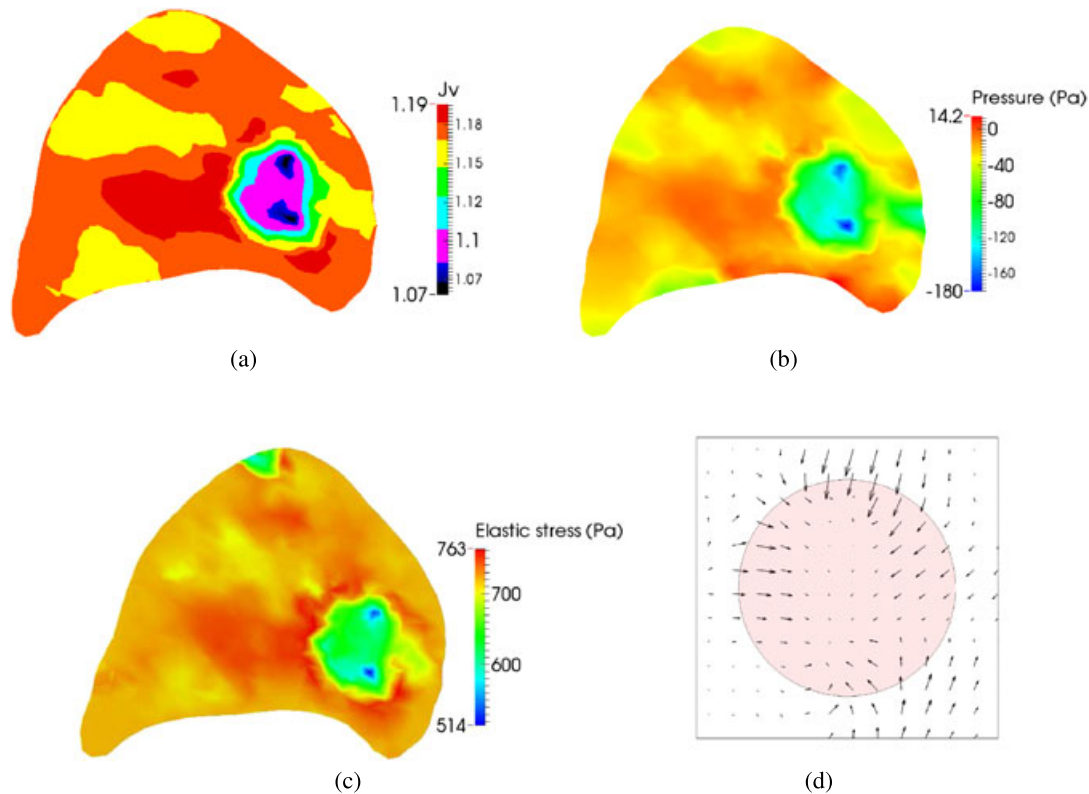
Figure 11. Effects in the sagittal slice of a 65% airway constriction within the modified region. (a) Relative Jacobian J_V, (b) tissue pressure, (c) elastic stress and (d) direction of the fluid flux near the structurally modified (constricted) region.

6.3. Breathing with locally reduced tissue elasticity

We simulate localised weakening of the tissue by reducing the Young's modulus of the tissue within the region represented by the red ball in Figure 5(b). We reduce the Young's modulus by 0%, 50%, 75% and 90%. This corresponds to a modified Young's modulus of 730, 365, 182.5 and 73 Pa, respectively.

Figure 12(a)–(c) plot the local expansion J_V, the pressure and the elastic stress within the modified region. As expected, local expansion increases as the tissue weakens, and the elastic stress decreases. Note that in all cases, the range (heterogeneity) of local ventilation, pressure and elastic stress within the modified region increases dramatically as the stiffness of the modified region decreases. In lung physiology, such regions are said to be hyper-inflated.

Due to the large amount of tissue expansion within the structurally modified region, the tissue immediately surrounding this region is effectively under-inflated between the expanded modified region and the surrounding tissue, and as a result, as seen in Figure 13, it is this region that expands the least.

6.4. Dynamic hysteresis

With the current choice of hyperelastic strain energy law (3) for the tissue mechanics, our model does not produce the classical hysteresis effects, which are attributed to the visco-elastic properties of the biological tissues involved, elastin and collagen, within lung tissue [26]. However, we observe dynamic hysteresis effects caused by delayed emptying and filling of different regions of the lung.

Figure 14(a) plots the total stress against lung volume throughout the breathing cycle for three different breathing rates. The pressure-volume (pV) curves indicate very different amounts of hysteresis at different breathing rates.
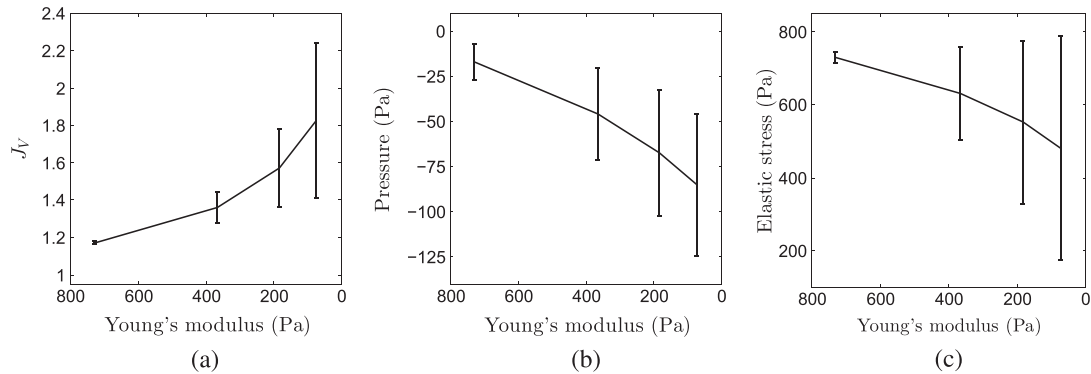
Figure 12. Effects of localised weakening of the tissue. Expansion, pressure and stress within the modified region vs Young's modulus within the structurally modified region. (a) Means and standard deviations of the relative Jacobian, (b) means and standard deviations of the tissue pressure and (c) means and standard deviations elastic stress.
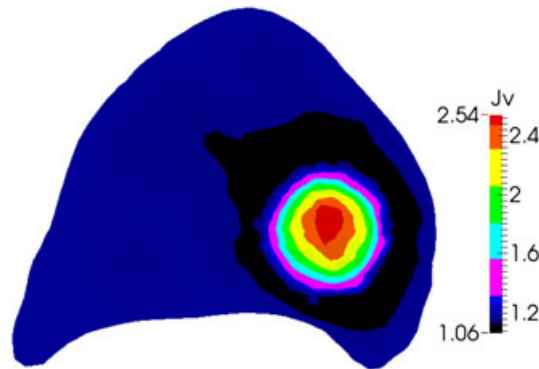

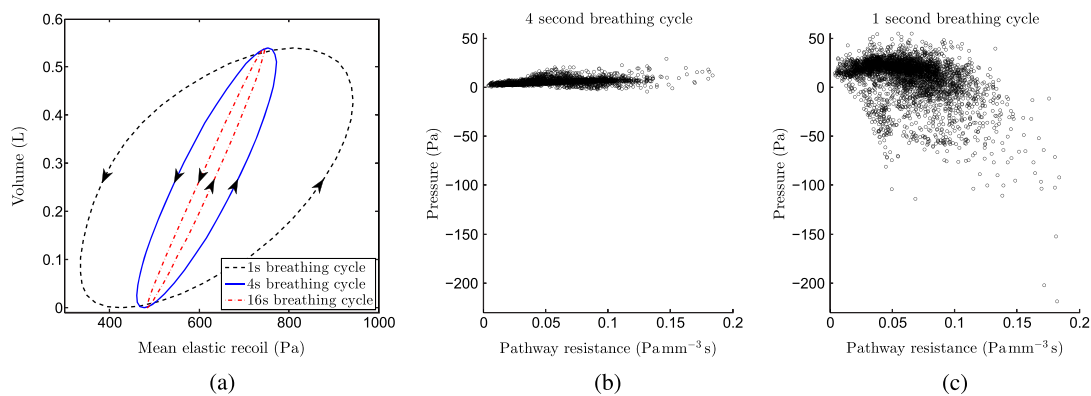Figure 13. Relative Jacobian during inspiration with 90% localised tissue weakening.

Figure 14. (a) Dynamic pressure–volume curve: mean elastic recoil (total stress) against lung tidal volume during one full breathing cycle, for three different breathing rates. The arrows indicate the direction of time during the breathing cycle. (b) Pathway resistance against pressure with a 4-s breathing cycle, 0.2 s after peak inhalation. (c) Pathway resistance against pressure with a 1-s breathing cycle, 0.05 s after peak inhalation.

Figure 14(b) and (c) shows the distribution of pressure against airway resistance shortly after the end of inhalation. At this point, the lung as a whole has started to exhale air. However, particularly at the faster breathing rate, some lung regions have a negative pressure and are still filling. These parts of the lung also tend to have a higher airway resistance and therefore to fill more slowly and are subject to expansive stresses due to the more highly ventilated (and therefore expanded)

tissue surrounding them. The negative pressures in the regions that are still filling near peak volume result in a larger total stress given by $\boldsymbol{\sigma} = \boldsymbol{\sigma}_e - p\boldsymbol{I}$, causing the curve to shift right when moving from inspiration to expiration (because of delayed filling) and left when moving from expiration to inspiration (because of delayed emptying). A faster breathing rate and therefore faster flow rates exaggerates this effect and causes an increased amount of hysteresis, that is, a widening of the dynamic PV curve in Figure 14(a). Because the work performed is proportional to the area enclosed by the pV diagram, considerably more work is required during more rapid breathing.

Figure 14(b) and (c) plots pressure against airway resistance for a 4-s and a 1-s breathing cycle, respectively. We observe an increased heterogeneity in the tissue's pressure distribution with increased breathing rate. The pressure differences between poorly ventilated and well-ventilated regions increase at high flow rates resulting in both an increase in stress (decrease in pressure) and an increase in heterogeneity of the total stress.

7. CONCLUSIONS AND FUTURE DIRECTIONS

We have presented a mathematical model of a generic human lung suitable for use in investigating the role of parenchymal mechanics in lung ventilation. The model tightly couples tissue deformation with ventilation by using a poroelastic model for the lung parenchyma coupled to an airway network model for the bronchial tree. We have highlighted the assumptions necessary to arrive at such a model. In contrast with many previous ventilation models, the current approach models the tissue as a continuum. Therefore, it is able to locally conserve mass (which means conserve volume as the solid skeleton and fluid are both incompressible), and to model collateral ventilation. Further, it is driven by deformation boundary conditions extracted from imaging data to avoid having to prescribe a pleural pressure that is impractical to measure experimentally. In simulations of normal breathing, the model is able to produce physiologically realistic global measurements and dynamics. In simulations with altered airway resistances and tissue stiffnesses, the model illustrates the interdependence of the tissue and airway mechanics and thus the importance of a fully coupled model. We have found that there is a strong correlation between airway resistance and the local mechanical properties of the tissue to ventilation (Figure 8(a)).

Because of heterogeneity in airway resistance, dynamic hysteresis effects appear during breathing (Figure 14(a)) and result in a complex ventilation distribution caused by delayed filling and emptying of the tissue. In particular, small changes in airway radii result in large changes in pathway resistance, which in turn can significantly affect ventilation and mechanical stresses within the lung. Furthermore, we have shown that reducing regional elastic properties of the tissue leads to areas of both hyper-inflation and under-inflation. Such physiological phenomenon are commonly seen within a diseased lung. Hence, by further refinement of the model, it is hoped that it will provide insight into diseases such as asthma and chronic obstructive pulmonary disease.

Future directions will aim to both incorporate further detail into the model, such as gas exchange, and provide patient-specific parameterisation of the model. Using the model in a patient-specific setting will require using imaging data, such as motion CT, to infer parameters for the hyperelastic strain energy law on a regional basis. Further, due to the inability of CT to resolve airways past approximately generation six, we have used an algorithmic method to generate the distal airways. The generated portion of the tree is not patient-specific, and radii will also have to be inferred from imaging data, such as hyperpolarized gas magnetic resonance imaging ventilation maps.

It is hoped that the model presented here can form the basis for studies on the importance of airway and tissue heterogeneity on lung function, testing of mechanical hypothesis for the progression of disease and investigations into phenomena such as hyperinflation, fibrosis and constriction.

REFERENCES

1. Ismail M, Comerford A, Wall WA. Coupled and reduced dimensional modeling of respiratory mechanics during spontaneous breathing. *International Journal for Numerical Methods in Biomedical Engineering* 2013; **29**(11): 1285–1305.
2. Swan A, Clark A, Tawhai M. A computational model of the topographic distribution of ventilation in healthy human lungs. *Journal of Theoretical Biology* 2012; **300**(0):222 –231.
3. Tawhai M, Lin C. Image-based modeling of lung structure and function. *Journal of Magnetic Resonance Imaging* 2010; **32**(6):1421–1431.
4. Lin C, Tawhai M, McLennan G, Hoffman E. Multiscale simulation of gas flow in subject-specific models of the human lung. *IEEE Engineering in Medicine and Biology Magazine* 2009; **28**(3):25–33.
5. Werner R, Ehrhardt J, Schmidt R, Handels H. Patient-specific finite element modeling of respiratory lung motion using 4d ct image data. *Medical physics* 2009; **36**(5):1500–1511.
6. Eom J, Xu X, De S, Shi C. Predictive modeling of lung motion over the entire respiratory cycle using measured pressure-volume data, 4DCT images, and finite-element analysis. *Medical physics* 2010; **37**(8):4389–4400.
7. Fuld M, Easley R, Saba O, Chon D, Reinhardt J, Hoffman E, Simon B. CT-measured regional specific volume change reflects regional ventilation in supine sheep. *Journal of Applied Physiology* 2008; **104**(4):1177–1184.
8. Lee G, Tseng N, Yuan Y. Finite element modeling of lungs including interlobar fissures and the heart cavity. *Journal of Biomechanics* 1983; **16**(9):679–690.
9. Kowalczyk P. Mechanical model of lung parenchyma as a two-phase porous medium. *Transport in Porous Media* 1993; **11**(3):281–295.
10. Owen M, Lewis M. The mechanics of lung tissue under high-frequency ventilation. *SIAM Journal on Applied Mathematics* 2001:1731–1761.
11. Suki B, Bates J. Lung tissue mechanics as an emergent phenomenon. *Journal of Applied Physiology* 2011; **110**(4):1111–1118.
12. Galbán CJ, Han MK, Boes JL, Chughtai KA, Meyer CR, Johnson TD, GalbÂt'an S, Rehemtulla A, Kazerooni EA, Martinez FJ et al. Computed tomography-based biomarker provides unique signature for diagnosis of COPD phenotypes and disease progression. *Nature Medicine* 2012; **18**(11):1711–1715.
13. Prange H. Laplace's law and the alveolus: a misconception of anatomy and a misapplication of physics. *Advances in Physiology Education* 2003; **27**(1-4):34–40.
14. Yin Y, Choi J, Hoffman EA, Tawhai MH, Lin CL. A multiscale MDCT image-based breathing lung model with time-varying regional ventilation. *Journal of Computational Physics* 2013; **244**:168–192.
15. Yin Y, Choi J, Hoffman EA, Tawhai MH, Lin CL. Simulation of pulmonary air flow with a subject-specific boundary condition. *Journal of Biomechanics* 2010; **43**(11):2159–2163.
16. Ochs M, Nyengaard JR, Jung A, Knudsen L, Voigt M, Wahlers T, Richter J, Gundersen HJG. The number of alveoli in the human lung. *American Journal of Respiratory and Critical Care Medicine* 2004; **169**(1):120–124.
17. Weichert L. Computational Modeling of Multi-field and Multi-scale Phenomena in Respiratory Mechanics. *PhD Thesis*, Technischen Universität München, 2011.
18. Lawrence Berkeley National Laboratory. LBNL LungLab Tour, 1995. (Available from: http://www.whywasteyourbreath.com/images.html) [Accessed on 2012].
19. Ben-Tal A. Simplified models for gas exchange in the human lungs. *Journal of Theoretical Biology* 2006; **238**(2): 474–495.
20. Pedley T, Schroter R, Sudlow M. The prediction of pressure drop and variation of resistance within the human bronchial airways. *Respiration Physiology* 1970; **9**(3):387–405.
21. Markert B. A constitutive approach to 3-d nonlinear fluid flow through finite deformable porous continua. *Transport in Porous Media* 2007; **70**(3):427–450.
22. Leary D, Winkler T, Braune A, Maksym GN. Effects of airway tree asymmetry on the emergence and spatial persistence of ventilation defects. *Journal of Applied Physiology* 2014; **117**(4):353–362.
23. Berger L, Bordas R, Kay D, Tavener S. *A Stabilized Finite Element Method for Nonlinear Poroelasticity*. In Review.
24. Coussy O. *Poromechanics*. John Wiley & Sons Inc, 2004.
25. Wriggers P. *Nonlinear Finite Element Methods*. Springer Verlag, 2008.
26. Kowalczyk P, Kleiber M. Modelling and numerical analysis of stresses and strains in the human lung including tissue-gas interaction. *European Journal of Mechanics - A/Solids* 1994; **13**(3):367–393.
27. Holmes M, Mow V. The nonlinear characteristics of soft gels and hydrated connective tissues in ultrafiltration. *Journal of Biomechanics* 1990; **23**(11):1145–1156.
28. Lai W, Mow V. Drag-induced compression of articular cartilage during a permeation experiment. *Biorheology* 1980; **17**(1-2):111.
29. Berger L, Bordas R, Kay D, Tavener S. *Stabilized Lowest Order Finite Element Approximation for Three-Field Poroelasticity*. to appear in SIAM J. Scientific Computing.
30. Fang Q, Boas DA. Tetrahedral mesh generation from volumetric binary and grayscale images. *Biomedical Imaging: From Nano To Macro, 2009. ISBI'09. IEEE International Symposium on*, IEEE: Boston, USA, 2009; 1142–1145.
31. Bordas R, Lefevre C, Veeckmans B, Pitt-Francis J, Fetita C, Kay D, Siddiqui S, Burrowes K. Development and validation of patient-based complete conducting airways models 2014. Preprint.
32. Freed AD, Einstein DR. An implicit elastic theory for lung parenchyma. *International Journal of Engineering Science* 2013; **62**:31–47.

33. West J. *Respiratory Physiology: The Essentials*. Lippincott Williams & Wilkins, 2008.
34. Zhang T, Orton NP, Mackie TR, Paliwal BR. Technical note: A novel boundary condition using contact elements for finite element based deformable image registration. *Medical Physics* 2004; **31**(9):2412–2415.
35. Lande B, Mitzner W. Analysis of lung parenchyma as a parametric porous medium. *Journal of Applied Physiology* 2006; **101**(3):926–933.
36. De Wilde R, Clement J, Hellemans J, Decramer M, Demedts M, Boving R, Van de Woestijne KP. Model of elasticity of the human lung. *Journal of Applied Physiology* 1981; **51**(2):254–261.
37. Cetti E, Moore A, Geddes D. Collateral ventilation. *Thorax* 2006; **61**(5):371–373.

SUPPORTING INFORMATION

Additional supporting information may be found in the online version of this article at the publisher's web-site.